

See discussions, stats, and author profiles for this publication at: <https://www.researchgate.net/publication/330148780>

# Flexure-Based Magnetically Levitated Dual-Stage System for High-Bandwidth Positioning

Article in IEEE Transactions on Industrial Informatics · January 2019

DOI: 10.1109/TII.2019.2890951

---

CITATIONS

6

READS

122

3 authors, including:



Haiyue Zhu

Agency for Science, Technology and Research (A\*STAR)

41 PUBLICATIONS 290 CITATIONS

[SEE PROFILE](#)



Tat Joo Teo

Massachusetts Institute of Technology

67 PUBLICATIONS 759 CITATIONS

[SEE PROFILE](#)

Some of the authors of this publication are also working on these related projects:



anti swing control [View project](#)

# Flexure-Based Magnetically Levitated Dual-Stage System for High-Bandwidth Positioning

Haiyue Zhu, *Member, IEEE*, Tat Joo Teo, *Member, IEEE*, and Chee Khiang Pang, *Senior Member, IEEE*

**Abstract**—Bandwidth is a critical specification for the motion positioning systems as fast response to reference and broadband disturbance rejection are highly desirable in industrial applications, e.g. 2D/3D scanning. This paper presents a parallel actuation dual-stage concept to enhance the bandwidth of the magnetically levitated (maglev) positioning system, which is realized by utilizing the compliant joints to construct a monolithic-cut flexure-based fine positioning stage within the primary maglev stage, hence turning such a dual-stage system into a fully cableless maglev system. An integrated design approach is employed to design the flexure-based secondary stage by optimizing both the mechanical parameters and the controller parameters, where various specifications, e.g., stability, performance, and saturation are considered under the proposed framework. Experimental results have shown that the prototype can achieve Root-Mean-Square Error (RMSE) of 43 nm in the principal axis even though the accuracy of the primary maglev stage is limited in micron-level due to the noise of capacitive sensors. Results also show that the developed prototype can significantly improve the closed-loop bandwidth of the maglev system from 20 Hz to around 200 Hz.

**Index Terms**—Bandwidth, dual-stage, flexure, magnetic levitation, nanopositioning, integrated design, parallel actuation.

## I. INTRODUCTION

MULTIPLE Degrees-Of-Freedom (multi-DOF) position ing is required in many precision applications [1], [2] within the industries of biotechnology, optics, materials, semiconductor, etc. In general, multi-DOF positioning systems are realized through three types of architectures, i.e., the serial, parallel, and the direct drive [3], where the last is viewed as the ideal architecture. Magnetic levitation technology provides a promising solution to realize direct-drive 6-DOF precision positioning without needs of any additional mechanical/fluid bearings for motion guiding, thus providing frictionless motion, zero contamination, and vacuum compatibility, etc. Magnetically levitated (maglev) motion systems can be realized by using either the Lorentz force principle [4], [5] or the

Manuscript received October 10, 2018; revised November 25, 2018; accepted December 18, 2018. This work was supported by ASTAR (Agency for Science Technology and Research), SERC Grant No 142 64 00040, Technology Development for Suppliers Development Initiative WP4: Wafer Handling Module for Complex Equipment.

H. Zhu is with the Mechatronics Group, Singapore Institute of Manufacturing Technology, Agency for Science, Technology and Research (A\*STAR), Singapore 638075 (e-mail:zhu\_haiyue@simtech.a-star.edu.sg).

T. J. Teo is with the Advanced Remanufacturing and Technology Centre, A\*STAR, Singapore 637143 (e-mail:daniel\_teo@artc.a-star.edu.sg).

C. K. Pang is with the Engineering Cluster, Singapore Institute of Technology, Singapore 138683 and also with Department of Electrical and Computer Engineering, National University of Singapore, Singapore 117583 (e-mail:justinpang@nus.edu.sg).

attraction/repulsion of electromagnetic force [6]. The former owns a linear force-current characteristic that permits better controllability, which is much desirable in precision positioning tasks. Both working principles are well demonstrated through the moving-magnet designs [7], [8] and moving-coil designs [9], [10]. Moving-magnet design offers a truly cableless maglev system while the mass of the levitated translator would be lighter in the case of the moving-coil design.

Halbach Permanent Magnet (PM) array is widely used in these multi-DOF maglev positioning systems [7], [9]–[12] due to its well distributed two-directional sinusoidal magnetic fields [13]. Subsequently, 2D Halbach PM arrays are proposed [9], [14], [15] to obtain three-directional fields within a single magnet array, which improves the power efficiency for large displacement operations. Multi-layers PCB coils are adopted [3] to extend the displacement of maglev system. Lately, Halbach PM array with square coil is proposed [16] to achieve the concept of unlimited planar displacement with supporting multiple translators concurrently operating above one coil array. The complexity of the prototype in [16] is much lower than the 2D Halbach PM array based systems with similar functions since it only requires 8-phase current to fully control the all 6-DOF positioning.

Although the executions of high precision 6-DOF motion are well demonstrated by the existing maglev positioning systems, positioning bandwidth is another critical specification for a motion system as accurate tracking of high frequency reference and broadband disturbance rejection are highly desirable. From the perspective of mechanical property, the achievable bandwidth of a maglev positioning system is mainly restricted by factors such as the structural resonance and levitation mass, where these two factors are a bit conflicted as the higher structural resonance in translator indirectly contributes to higher mass, which is not favorable for high bandwidth applications when considering the power consumptions. From past literature, the reported bandwidths from existing 6-DOF maglev planar positioners include 35 Hz in [15], 38 Hz in [16] and [17], 50 Hz in [18], 85.8 Hz in [19], 95 Hz in [20], and 110 Hz in [11] etc. Compared with other motion systems, piezoelectric actuation motion systems can achieve several thousand Hz bandwidth while the Lorentz actuation (voice coil) systems can deliver several hundred Hz, which are much higher than the existing maglev motion systems. Pursuing higher closed-loop bandwidth is important to facilitate its real industrial adoption, and various efforts are made in this area through the better controller or mechanical design [21], [22].

In this work, a maglev dual-stage positioning system is employed to improve the maglev motion bandwidth whereby the

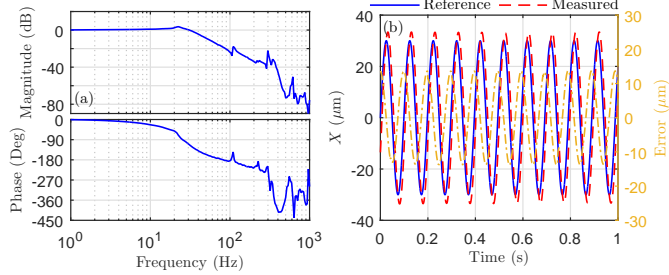


Fig. 1. (a) The closed-loop frequency response (from reference to output) of the planar motion in maglev motion stage [16] and (b) tracking performance for 10 Hz sinusoidal reference, where both experiments are conducted when levitating at 1 mm.

secondary stage is driven by a direct-drive Lorentz motor. Unlike a traditional dual-stage system that directly mounts a full secondary stage onto the primary stage, the proposed design adopts a novel parallel actuation dual-stage configuration [23] that utilized the compliant joints to construct a monolithic-cut flexure-based moving stage for both primary and secondary stages within one levitating platform. Hence, the translator is fully cable-less since there is no power cable attached to the secondary stage and thus preserves the contact-less nature of maglev technology. To design the secondary stage with desired specifications systematically, an integrated design approach is carried out, where multiple specifications are represented via convex constraints to optimize the system performance, e.g., robust stability, robust performance, and saturation avoidance. Through this approach, both the plant modal parameters and controller can be simultaneously optimized to improve the overall performance of the proposed maglev system.

The rest of the paper is organized as follows. The description of the proposed maglev dual-stage system is given in Section II and Section III presents the integrated design approach, the design of the secondary stage is presented in Section IV and Section V shows the experimental results of the developed prototype, and finally, a conclusion is drawn in Section VI.

## II. MAGLEV DUAL-STAGE POSITIONING

It is well documented that a maglev system can perform high-precision multi-DOF motion due to its friction-less and contact-less nature. On the other hand, the control bandwidth of a maglev system is limited by the low resonant frequency and large levitation mass. Fig. 1(a) plots the closed-loop frequency response from reference to output of the planar motion for a maglev motion stage [16]. (Note: [16] uses laser interferometer for  $X$  and  $Y$ -axis measurements, which is different from the maglev primary stage as shown in Fig. 2). It shows that the closed-loop bandwidth is close to 38 Hz. Fig. 1(b) plots the experiment of a 10 Hz sinusoidal reference for the above maglev prototype. As can be seen, the recorded errors are relatively large due to the phase lag and the positioning performance is limited by the low bandwidth of this motion system.

The maglev dual-stage configuration is employed in this work to enhance the bandwidth of maglev positioning. Fig. 2

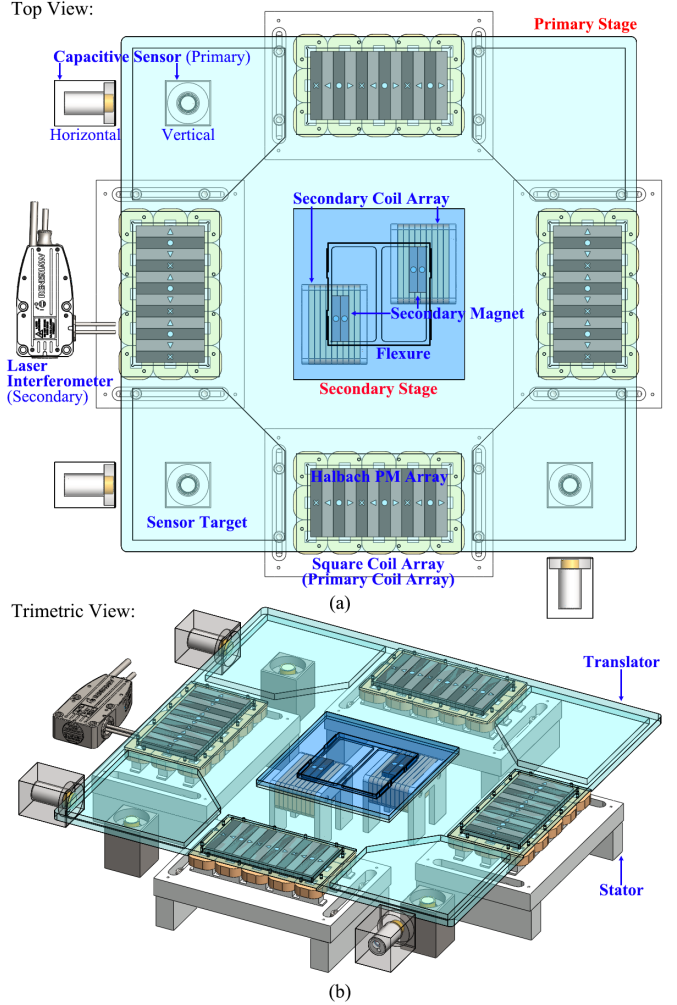


Fig. 2. The concept of the proposed maglev dual-stage configuration: (a) top view and (b) trimetric view.

shows the concept of the proposed parallel actuation dual-stage configuration, where a 6-DOF maglev motion stage is utilized to provide the primary motion while the secondary stage is a single-axis Lorentz motion system with its moving part being supported by the flexure-based bearings that are connected back to the primary stage. Unlike the traditional series actuation design, the proposed configuration employs a single monolithic-cut flexure-based translator to form both the primary and secondary stages, while the actuation coils for both stages are laid underneath as one single coil stator fixed on the base. As a result, only the moving part of secondary stage is connected with the primary maglev translator via the compliant joints. The advantages of this parallel actuation dual-stage design include: 1) truly contact-less maglev system where no cables are attached to the levitated translator for powering the secondary stage and 2) provides a lower levitating mass since the actuation coils are no longer moving together with the translator.

### A. Maglev Primary Stage

In the primary maglev stage, the floating translator consists of four 1D Halbach arrays, where the magnetization direction of each Halbach PM array is illustrated in Fig. 3(a). Due to this special arrangement, each Halbach PM array generates a 2D sinusoidal magnetic flux that concentrates only to one side of the array. The stator of the primary maglev stage includes four coil arrays, which are located below the Halbach PM arrays to generate the horizontal ( $X$  or  $Y$ ) and vertical ( $Z$ ) force. The schematics of the actuation of each forcer is shown in Fig. 3(a). The current in the coils are controlled within two phases ( $I_1$  and  $I_2$ ) so that the desired levitation and propulsion forces can be generated on each forcer to enable the primary stage to provide 6-DOF positioning. The force modeling of this maglev stage is detailed in [16]. In theory, this design can achieve unlimited-stroke planar motion if the square coils spread full of the workspace. In this work, the 6-DOF motion of primary stage is sensed by six channels of capacitive sensors, i.e., three for the vertical displacements and the remaining three for the horizontal displacements as shown in Fig. 2. Hence, the actual displacement range is limited by the measurement range of the capacitive sensor, which is less than 5 mm.

Another reason to choose the capacitive sensor for the primary stage is to evaluate whether a secondary stage can still achieve high positioning resolution if the primary stage uses a low-resolution sensor. The signal of capacitive sensor is relatively noisy with peak-to-peak resolution of  $1\mu\text{m}$ . The proposed maglev dual-stage system should demonstrate that the dual-stage system can still achieve a much high positioning resolution even if the primary stage uses low resolution sensors. This issue is important for the practical consideration that a high resolution 6-DOF sensing system is always costly, especially for the large displacement. With the proposed dual-stage system, low-cost sensing system [3], [24] can be used for the primary stage to achieve large displacement range transportation while high positioning resolution in the processing area can still be achieved via the secondary stage.

### B. Flexure Secondary Stage

In this work, the secondary stage is a 1-DOF Lorentz-force motion system. The reason for choosing 1-DOF instead of 2-DOF planar motion is due to the consideration of the raster scan trajectory for scanning processes, which is most widely

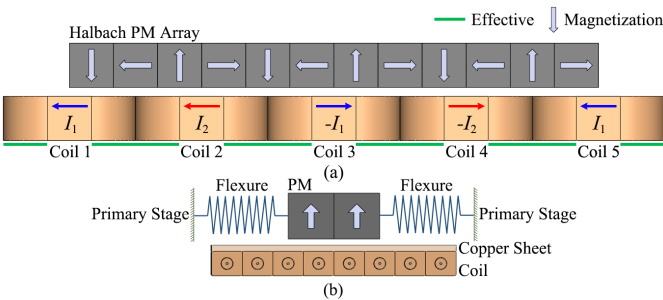


Fig. 3. The actuation schematics of (a) primary and (b) secondary stages.

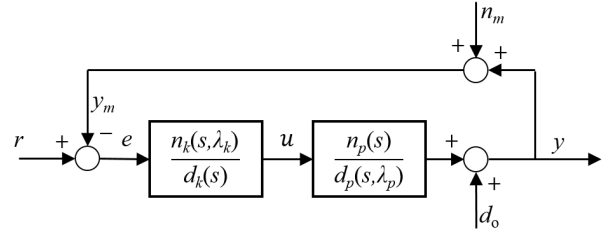


Fig. 4. Negative output feedback configuration with output disturbance and measurement noise.

used in real applications due to its simplicity [25]. The raster trajectory conducts the region scanning line by line, one axis moves one step only when the other axis completed one single line scan. Hence, improving the bandwidth and dynamics in one axis can greatly enhance the scanning performance for a planar motion stage. Here, this axis is denoted as the principal axis.

In this work, the objective of the secondary stage is to enhance the bandwidth of the principal axis. The working principle of the secondary stage is shown in Fig. 3(b) where the moving part contains the magnets and the stationary part is the single-phase coil arrays, and the secondary stage is actuated by the generated Lorentz force. The detailed mechanical design can be seen in Fig. 2. The moving platform of the secondary stage is carried by the primary translator using the flexure joints, which is a simple four-beam mechanism (see Fig. 7 for details). Two magnets are installed on the flexure platform with dimension of  $40\text{ mm} \times 15\text{ mm} \times 7.5\text{ mm}$ , and the coil arrays with top surface of  $45\text{ mm} \times 70\text{ mm}$  are placed accordingly with series connection. By controlling the magnitude of current in the coil array, corresponding Lorentz force will be generated to actuate the motion of secondary stage. Consequently, the merits of the secondary flexure stage include large stiffness, high resonance frequency, and zero-commutation, which is supposed to enhance the bandwidth and dynamics for the overall positioning. The flexure-based secondary stage can be represented as a second-order system,

$$G_s(s) = \frac{g_s}{m_s s^2 + d_s s + k_s}, \quad (1)$$

where  $m_s$  denotes the lumped mass of secondary stage,  $d_s$  is the effective damping,  $k_s$  represents the system stiffness, and  $g_s$  is the system gain. The function of this Lorentz motor in the maglev dual-stage system is to further reduce the tracking error for the maglev stage. Hence, the parameters in (1) should be carefully designed to achieve good performance. An integrated design and control approach is proposed to obtain the mechanical parameters and controller parameters concurrently, which is presented in the subsequent sections.

### III. INTEGRATED DESIGN APPROACH

The framework to carry out the integrated design approach is a negative output feedback configuration as shown in Fig. 4, which includes a plant  $P(s)$  and a controller  $K(s)$ . Without loss of generality, assuming the mechanical plant to be designed

is a Single-Input-Single-Output (SISO) Linear Time-Invariant (LTI) system, and in continuous time, it is represented as,

$$\begin{aligned} P(s) &= \frac{n_p(s)}{d_p(s)} = N_p(s)D_p(s, \lambda_p)^{-1}, \\ N_p(s) &= \frac{n_p(s)}{d_{cp}(s)}, \text{ and } D_p(s, \lambda_p) = \frac{d_p(s, \lambda_p)}{d_{cp}(s)}, \end{aligned} \quad (2)$$

where  $n_p(s)$  and  $d_p(s)$  are the numerator and denominator polynomials of the plant  $P(s)$ ,  $d_{cp}(s)$  is a Schur polynomial with the same order as  $d_p(s)$ , and  $N_p(s)D_p(s)^{-1}$  is the coprime factorization representation of the plant. Let  $\lambda_p$  denotes a vector of the design parameters to be determined in the integrated design approach, and the assumption is made that the design parameters in  $\lambda_p$  are located affinely in either plant numerator or denominator, i.e.,  $n_p(s, \lambda_p)$  or  $d_p(s, \lambda_p)$ . For example,  $\lambda_p$  is the coefficient vector of the polynomial  $d_p(s, \lambda_p)$ . For the practical consideration in this work, it is assumed the design parameters vector  $\lambda_p$  is on plant denominator polynomials  $d_p(s, \lambda_p)$  in further derivation.

In practice, the uncertainties and perturbations in design parameters of  $\lambda_p$  are unavoidable for the real systems due to the manufacturing and assembly errors. These perturbations can be represented by the interval uncertainties, i.e.,  $\lambda_p \in [\lambda_p^l, \lambda_p^u]$ . Consequently, the perturbed  $P(s)$  due to the interval uncertainties can be captured by the polytopic system, that  $P_i(s) = n_p(s)/d_{ip}(s, \lambda_p) = N_p(s)D_{ip}(s, \lambda_p)^{-1}$  denotes its  $i$ th vertex,  $i = 1, 2, \dots, v$ , where  $v$  denotes the number of all possible vertices, so that the set of all possible  $P(s)$  in this polytopic system can be represented by

$$\begin{aligned} \mathcal{P} : \left\{ P(s) = N_p(s)D_p(s, \lambda_p)^{-1} \middle| \mu_i \geq 0, \sum_{i=1}^v \mu_i = 1, \right. \\ \left. D_p(s, \lambda_p) = \sum_{i=1}^v \mu_i D_{ip}(s, \lambda_p) \right\}. \end{aligned} \quad (3)$$

Using the structure of standard negative feedback configuration, shown as Fig. 4, consider an output feedback controller

$$\begin{aligned} K(s) &= \frac{n_k(s, \lambda_k)}{d_k(s)} = N_k(s)D_k(s)^{-1}, \\ N_k(s) &= \frac{n_k(s, \lambda_k)}{d_{ck}(s)}, \text{ and } D_k(s) = \frac{d_k(s)}{d_{ck}(s)}, \end{aligned} \quad (4)$$

where  $n_k(s, \lambda_k)$  is numerator polynomial of the controller with affine design parameters  $\lambda_k$ ,  $d_k(s)$  is a fixed denominator polynomial of the controller,  $d_{ck}(s)$  is a Schur polynomial with the same order as  $d_k(s)$ , and  $N_k(s)D_k(s)^{-1}$  is the coprime factorization representation of the controller. The resulted sensitivity, complementary sensitivity, and input sensitivity transfer functions of the closed-loop system for  $P(s) \in \mathcal{P}$  are expressed as

$$\begin{aligned} S(s) &= \frac{D_p(s, \lambda_p)D_k(s)}{N_p(s)N_k(s, \lambda_k) + D_p(s, \lambda_p)D_k(s)}, \\ T(s) &= \frac{N_p(s)N_k(s, \lambda_k)}{N_p(s)N_k(s, \lambda_k) + D_p(s, \lambda_p)D_k(s)}, \\ U(s) &= \frac{D_p(s, \lambda_p)N_k(s, \lambda_k)}{N_p(s)N_k(s, \lambda_k) + D_p(s, \lambda_p)D_k(s)}. \end{aligned} \quad (5)$$

It is noted that the design parameters  $\lambda_p, \lambda_k$  affinely locate on both the numerator and denominator polynomials of the sensitivity and complementary sensitivity transfer functions. Furthermore, in three components of coprime factors  $N_pN_k(\lambda_k)$ ,  $D_p(\lambda_p)D_k$ , and  $N_pN_k(\lambda_k) + D_p(\lambda_p)D_k$ , the design parameters  $\lambda_p$  and  $\lambda_k$  are only located in the numerator polynomials while the denominator is fixed as constant polynomials.

The integrated design approach is performed on the objective to achieve desired closed-loop specifications by carrying out a convex optimization. The optimization is formulated as

$$\begin{aligned} \min_{\lambda_p, \lambda_k} \rho \\ \text{subject to:} \\ \text{Robust Stability} \\ \text{Robust Performance} \end{aligned} \quad (6)$$

where  $\rho$  is performance index to be optimized and the *Robust Stability*, and *Robust Performance* denote the desired performance specified on the closed loop for the polytopic system  $P(s) \in \mathcal{P}$  via convex constraints, which will be discussed in following.

#### A. Robust Stability

For the control systems, the stability is the most important issue to ensure. The robust stability of the closed loop in the polytopic system can be expressed by the following theorem.

*Theorem 1:* Consider a plant  $P(s)$  defined in the polytopic representation (3), the set of all  $\lambda_p$  and  $\lambda_k$  that stabilizes the closed-loop systems for all  $P(s) \in \mathcal{P}$  is given by

$$\Lambda : \left\{ \lambda_p \text{ and } \lambda_k \middle| N_p(s)N_k(s, \lambda_k) + D_{ip}(s, \lambda_p)D_k(s) \in \mathcal{S} \right. \\ \left. \text{for every } i = 1, 2, \dots, v \right\}, \quad (7)$$

where  $\mathcal{S}$  denotes the set of all positive realness transfer function.

*Proof:* To show that the set of all  $\lambda_p$  and  $\lambda_k$  stabilizes the entire polytope of  $P(s)$ , it is noted that the denominator of (5)

$$\begin{aligned} &N_p(s)N_k(s, \lambda_k) + D_p(s, \lambda_p)D_k(s) \\ &= N_p(s)N_k(s, \lambda_k) + \left( \sum_{i=1}^v \mu_i D_{ip}(s, \lambda_p) \right) D_k(s) \\ &= \sum_{i=1}^v \mu_i (N_p(s)N_k(s, \lambda_k) + D_{ip}(s, \lambda_p)D_k(s)). \end{aligned} \quad (8)$$

Since  $N_p(s)N_k(s, \lambda_k) + D_{ip}(s, \lambda_p)D_k(s)$  is ensured in (7), this directly leads to  $N_p(s)N_k(s, \lambda_k) + D_p(s, \lambda_p)D_k(s) \in \mathcal{S}$  as  $\mu_i \geq 0$ , which indicates all  $\lambda_p$  and  $\lambda_k$  that stabilizes the closed-loop systems for all  $P(s) \in \mathcal{P}$  according to the positive realness property. ■

Numerically, the positive realness condition in (7) can be guaranteed by the convex constraint for every vertex using the positive realness lemma [26].

### B. Robust Performance

Beside the stability, performance is the important aspect for high-precision motion systems, which includes disturbance rejection, bandwidth, etc. The robust performance of the closed loop for the polytopic system can be expressed by the following theorem.

*Theorem 2:* Consider a plant  $P(s)$  defined in the polytopic representation (3), the set of all  $\lambda_p$  and  $\lambda_k$  that satisfy the finite-frequency specification  $|S(j\omega)| < \rho$ , for all  $P(s) \in \mathcal{P}$  and  $\omega \in \Omega$ , is given by

$$\begin{aligned} \Lambda : & \left\{ \lambda_p \text{ and } \lambda_k \mid \text{for every } i = 1, 2, \dots, v : \right. \\ & \left| D_{pi}(j\omega, \lambda_p) D_k(j\omega) \right| < (1 - \delta)\rho, \quad \omega \in \Omega; \\ & \left. \left| N_p(j\omega) N_k(j\omega, \lambda_k) + D_{pi}(j\omega, \lambda_p) D_k(j\omega) - 1 \right| < \delta, \quad \omega \in \Omega \right\}, \end{aligned} \quad (9)$$

where  $\Omega$  denotes a finite-frequency range and  $\delta$  is a constant that  $\delta \in (0, 1)$ .

*Proof:* To show that the set of all  $\lambda_p$  and  $\lambda_k$  satisfy the finite-frequency specification  $|S(j\omega)| < \rho$ ,  $\omega \in \Omega$ , for the entire polytope of  $P(s)$ , it is noted

$$\begin{aligned} \left| D_p(j\omega, \lambda_p) D_k(j\omega) \right| &= \left| \left( \sum_{i=1}^v \mu_i D_{pi}(s, \lambda_p) \right) D_k(s) \right| \\ &= \sum_{i=1}^v \mu_i \left| D_{pi}(j\omega, \lambda_p) D_k(j\omega) \right| < (1 - \delta)\rho, \quad \text{for all } \omega \in \Omega. \end{aligned} \quad (10)$$

Furthermore, it is also noted that

$$\begin{aligned} & \left| N_p(j\omega) N_k(j\omega, \lambda_k) + D_p(j\omega, \lambda_p) D_k(j\omega) \right| \\ &= \left| N_p(j\omega) N_k(j\omega, \lambda_k) + \left( \sum_{i=1}^v \mu_i D_{pi}(j\omega, \lambda_p) \right) D_k(j\omega) \right| \\ &= \sum_{i=1}^v \mu_i \left| N_p(j\omega) N_k(j\omega, \lambda_k) + D_{pi}(j\omega, \lambda_p) D_k(j\omega) \right|. \end{aligned} \quad (11)$$

According to the last condition of (9), it is noted that  $1 - \delta < |N_p(j\omega) N_k(j\omega, \lambda_k) + D_{pi}(j\omega, \lambda_p) D_k(j\omega)| < 1 + \delta$ , for all  $\omega \in \Omega$ , which implies that,

$$1 - \delta < |N_p(j\omega) N_k(j\omega, \lambda_k) + D_p(j\omega, \lambda_p) D_k(j\omega)| < 1 + \delta, \quad \text{for all } \omega \in \Omega. \quad (12)$$

Consequently, using the results of (10) and (12),

$$|S(j\omega)| = \left| \frac{D_p(j\omega, \lambda_p) D_k(j\omega)}{N_p(j\omega) N_k(j\omega, \lambda_k) + D_p(j\omega, \lambda_p) D_k(j\omega)} \right| < \rho, \quad (13)$$

for all  $\omega \in \Omega$ . ■

Numerically, the finite-frequency bounded realness condition in (9) can be guaranteed by the convex constraints for every vertex using the Generalized KYP lemma [27]. Base on the above result, various robust performance specifications can be considered in the integrated design approach.

### C. Saturation Avoidance Scheme

Input saturation is a common problem for the control system. To avoid the input saturation but maintain certain closed-loop performance as discussed previously, a reasonable way is to lower the controller gain but to boost the plant gain, so that the small input generated from the low-gain controller can generate large output as well, and the open-loop gain remains unchanged to satisfy the control performance. Physically, this relates to enhance the mechanical advantage of a plant. In this work, the saturation avoidance scheme is proposed to optimally allocate the gains of both the plant and controller.

The control input is related to the input sensitivity transfer function  $U(s)$  as defined in (5), for the bounded reference  $|r(t)|_\infty < \delta_r$ ,

$$u(t) = \int_{-\infty}^{+\infty} U(\tau) r(t - \tau) d\tau, \quad (14)$$

so that

$$|u(t)| = \left| \int_{-\infty}^{+\infty} U(\tau) r(t - \tau) d\tau \right| \leq \delta_r \int_{-\infty}^{+\infty} |U(\tau)| d\tau. \quad (15)$$

As a result,

$$|u(t)|_\infty \leq \delta_r |U(s)|_1, \quad (16)$$

where  $|U(s)|_1 = \int_{-\infty}^{+\infty} |U(\tau)| d\tau$ , and  $|\cdot|_1$  denotes the  $L_1$ -norm of  $U(s)$ . In this work, the property of the  $L_1$ -norm in (16) of  $U(s)$  is utilized in the integrated design to achieve the saturation avoidance for the mechatronics design.

Although the design parameters  $\lambda_p$  and  $\lambda_k$  are already solved from the optimization (6), it is noted that as long as the product of the  $n_p(s)$  and  $n_k(s)$  remains constant, the specifications on  $S(s)$  and  $T(s)$  as formulated previously will be not changed. In view of this, the relocation scheme for the saturation avoidance is achieved by let  $n'_p(s) = g_0 n_p(s)$  and  $n'_k(s) = n_k(s)/g_0$ , where  $n'_p(s)$  and  $n'_k(s)$  are the reallocated gains of plant and controller, respectively. The scheme to determine the suitable  $g_0$  that can satisfy the  $L_1$ -norm specification on the input sensitivity transfer function  $U(s)$  is to ensure

$$\left| \frac{d_p(s) n_k(s)/g_0}{n_p(s) n_k(s) + d_p(s) d_k(s)} \right|_1 < \xi, \quad (17)$$

where  $\xi$  is a constant determined by the input drive device, so that the control input  $u(t)$  will be bounded by  $\xi \delta_r$ . Numerically, the  $L_1$ -norm specification in (17) can be guaranteed by the convex constraints [28]. As the plant  $P(s)$  is captured by a polytopic representation (3), the robust  $L_1$ -norm specification can be ensured by satisfying the specification on every vertex.

## IV. DESIGN OF FLEXURE SECONDARY STAGE

In this section, the proposed integrated design in last section is utilized to design the secondary Lorenz motion system. Following up to (1) and (2), the model of secondary stage can be written as,

$$G_s(s) = \frac{g_s k_s}{m_s s^2 + d_s s + k_s} = \frac{n_p}{d_p(\lambda_p)}, \quad (18)$$

where the mass  $m_s$  can be considered as known that  $m_s = 0.18$  kg, which is determined from the mechanical dimension,

and the integrated design approach will be used to search the optimal mechanical parameters and controller parameters for the secondary stage. In practical, the parameter perturbations are unavoidable for the real mechanical system, and to capture such uncertainties,  $d_s$  and  $k_s$  are represented in the interval,

$$\begin{aligned} d_s &\in [(1 - \Delta_d)\bar{d}_s, (1 + \Delta_d)\bar{d}_s] \\ k_s &\in [(1 - \Delta_k)\bar{k}_s, (1 + \Delta_k)\bar{k}_s], \end{aligned} \quad (19)$$

where  $\bar{d}_s$  and  $\bar{k}_s$  denote the central values of the  $d_s$  and  $k_s$ ,  $\Delta_d$  and  $\Delta_k$  represent the allowable perturbation level, and  $\Delta_d$  and  $\Delta_k$  are set as 3%. The controller for the secondary stage is a second-order controller with the structure

$$K_s(s) = \frac{k_0 s^2 + k_1 s + k_2}{s(s + T_d)} = \frac{n_k(\lambda_k)}{d_k}, \quad (20)$$

where it is actually a PID controller with low-pass filter,  $T_d$  is the filter constant that  $T_d = 2\pi 200$ , and  $k_0$ ,  $k_1$ , and  $k_2$  are the controller parameters in  $\lambda_k$  to obtain from the design approach.

The following specifications are employed to design the Lorenz motor, i.e., stability, bandwidth, and high frequency roll-off. To ensure the stability of the system (1) and (20) under uncertainty of (19), the specification can be represented by (7) according to Theorem 1,

$$\frac{n_p n_k(\lambda_k) + d_{pi}(\lambda_p) d_k}{d_c} \in \mathcal{S}, \quad (21)$$

where  $i = 1, 2, 3$ , and 4 as there are two parameters with uncertainties, and  $d_c = d_{cp} d_{ck}$  is selected as

$$d_c = s^4 + 1.2e3s^3 + 1.2e6s^2 + 2e8s + 8e10, \quad (22)$$

which is selected based on the desired closed-loop characteristics that has a pair of dominant poles in  $-56.57 \pm 277.59i$  related to the dynamics response.

Next, to maximize the bandwidth  $\omega_{bs}$ , defined as the maximal  $\omega$  that  $S(j\omega) < -3$  dB, the specification is chosen according to (9) of Theorem 2,

$$\begin{aligned} \left| \frac{d_{pi}(\lambda_p) d_k}{d_c} \right| &< (1 - \delta) \rho_b, \quad \omega \in (\omega_{bsl}, \omega_{bsh}), \\ \left| 1 - \frac{n_p n_k(\lambda_k) + d_{pi}(\lambda_p) d_k}{d_c} \right| &< \delta, \quad \omega \in (\omega_{bsl}, \omega_{bsh}), \end{aligned} \quad (23)$$

where  $\rho_b$  is the optimization index and  $\delta = 0.5$ . Here,  $\omega_{bsl}$  and  $\omega_{bsh}$  are chosen as  $2\pi 1$  and  $2\pi 40$ , respectively.

The next specification is to roll-off  $T(s)$  to avoid the excitation of unmodelled resonances in high frequency. Similarly, this roll-off condition can be expressed by

$$\begin{aligned} \left| \frac{n_k(\lambda_k)}{d_c} \right| &< (1 - \delta) \mu_{ro}, \quad \omega \in (\omega_h, +\infty), \\ \left| 1 - \frac{n_p n_k(\lambda_k) + d_{pi}(\lambda_p) d_k}{d_c} \right| &< \delta, \quad \omega \in (\omega_h, +\infty), \end{aligned} \quad (24)$$

where  $\mu_{ro}$  is a known constant -3 dB, and  $\omega_h$  is selected as  $2\pi 800$ .

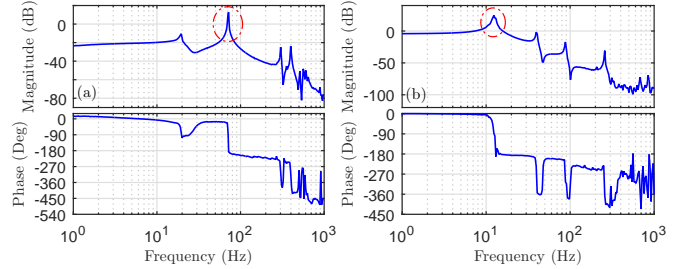


Fig. 5. Comparison of the levitated secondary stages' frequency responses with (a) rigid flexure and (b) soft flexure.

**1) Feasible Range of Flexure Stiffness:** Due to the floating property of the maglev motion, the maglev dual-stage system is more sensitive than conventional dual-stage systems. By adopting the parallel actuation scheme, the secondary stage will produce a coupling force to the maglev motion system via the flexure connection. As a result, if the flexure stiffness is too rigid, the closed-loop dynamics of the maglev primary stage will be introduced to the secondary stage, and vice versa. Fig. 5 plots the phenomenon comparison of the secondary stage frequency response in two cases: (a) is a rigid flexure with about 70000 N/m and (b) is a soft flexure with about 3000 N/m, where both cases are measured when the maglev primary stage is levitated up in same height with same controller setting. The red circles indicate the secondary stages' primary mechanical resonant modes. From Fig. 5(a), it can be observed that before the mechanical resonant mode in red circle, there is another resonance which is due to the closed-loop dynamics of maglev primary stage, and this changes the secondary stage's response significantly and will make it hard to control. However, in Fig. 5(b), such resonance around 20 Hz doesn't appear, and the frequency response almost doesn't change when levitated on or off. In this case, to avoid the undesired dynamics change when levitated up, the flexure stiffness should be restricted by an upper bound that  $k_s < \bar{k}_s$ ,  $\bar{k}_s = 20000$  N/m, to limit the coupling force less than 10 N.

**2) Feasible Range of Stage Damping:** The mechanically realize the designed damping coefficient, a copper sheet can be placed above the coil in the secondary stage, so that it can provide controllable damping by changing the thickness of the copper sheet using the eddy current principle. Similarly, the parameter  $d_s$  has a bound that  $\underline{d}_s < d_s < \bar{d}_s$ , where  $\underline{d}_s = 8$  Ns/m and  $\bar{d}_s = 10$  Ns/m. Overall, the restrictions for the stiffness and damping are,

$$\begin{aligned} k_s &< \bar{k}_s \\ \underline{d}_s &< d_s < \bar{d}_s. \end{aligned} \quad (25)$$

Finally, an optimization is created to search the optimal parameters by considering the mentioned specifications and restrictions, which is formulated as

$$\begin{aligned} \min_{(\lambda_p \text{ and } \lambda_k)} \rho_b \\ \text{subject to:} \\ (21), (23), (24) \text{ and (25).} \end{aligned} \quad (26)$$

TABLE I  
SOLVED DESIGN PARAMETERS FROM OPTIMIZATION (26).

Parameter	$m_s$	$d_s$	$k_s$	$g_s$
Value	0.18 kg	0.91 N·s/m	9.69e3 N/m	0.10 N/A
Parameter	$k_0$	$k_1$	$k_2$	
Value	2.205e2	2.996e4	1.529e07	

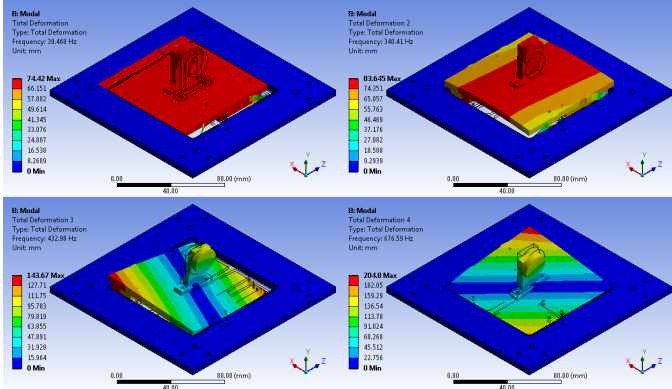


Fig. 6. Modal analysis of the designed flexure platform by FEA simulation.

The optimization (26) is solved by YALMIP Toolkit using SDPT3 solver in Matlab environment to obtain the design parameter vectors  $\lambda_p$  and  $\lambda_k$  in (1) and (20) accordingly. However, the optimization (26) only determine product term  $n_p n_k$  as appeared in the  $T(s)$  and  $S(s)$ . The allocation of  $n_p$  and  $n_k$  relies on the saturation avoidance scheme as introduced in (17). Finally, the solved mechanical plant and controller are listed as,

$$G_s(s) = \frac{9.754e2}{0.18s^2 + 0.91s + 9.69e3}, \quad (27)$$

and

$$C_s(s) = \frac{2.205e2s^2 + 2.996e4s + 1.529e07}{s(s + 1.2566e3)}, \quad (28)$$

where the corresponding values of the design parameters are listed in Table. I.

In this case, the  $L_1$  norm of the input sensitivity  $U_s(s) = \frac{C_s(s)}{1+G_s(s)C_s(s)}$  of (27) and (28) is calculated as 850, and it indicates that the upper bound of the controller input for 10  $\mu\text{m}$  stroke will be limited by 8.5 A, which is within the amplifiers' capabilities. It is also noted that the  $L_1$  norm is quite conservative for input saturation as it considers the extreme conditions, and this doesn't mean the secondary stage needs 8.5A for driving 10  $\mu\text{m}$  statically. In practical, the current for actuating full range of the secondary stage is less than 1 A.

To realize the obtained transfer function of secondary stage (27) into a real mechanical system, a flexure mechanism is carried out to achieve the desired stiffness  $k_s$  for the secondary stage. In this work, as the flexure mechanism for the maglev dual-stage system is 1-DOF and only requires for a small stroke of  $\pm 0.4$  mm to further reduce the tracking error of maglev motion stage, the proposed design utilizes a standard four-beam flexure, which all beams are parallel located. The length, thickness, and height of each beam are

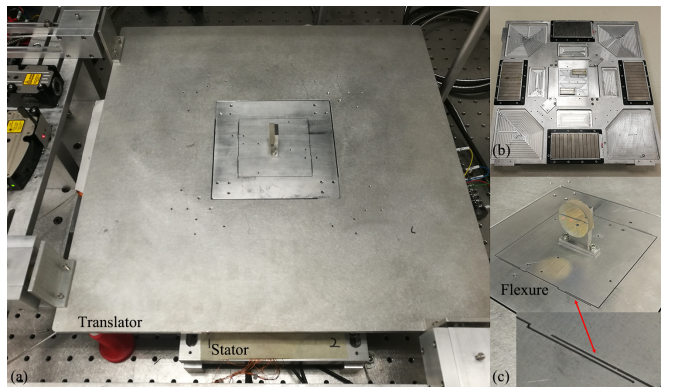


Fig. 7. (a) Photo of the proposed maglev dual-stage system, (b) bottom view of the translator, and (c) secondary stage.

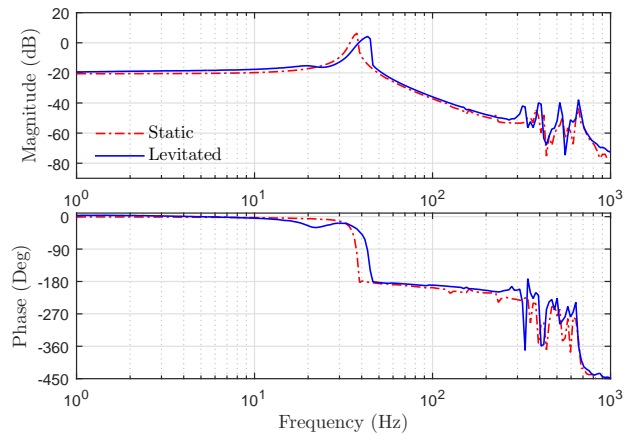


Fig. 8. Frequency response of the secondary flexure stage.

designed as 20.5 mm, 0.4 mm, and 5 mm, respectively, and the material is Aluminum 7075-T6. Fig. 6 shows the FEA modal analysis for the designed flexure platform, where the first four resonance modes are plotted. It indicates that the primary resonant mode is close to (27), and the second and upper resonance frequency are at least 3 times higher than the primary resonance frequency, which will help to eliminate the unwanted motions in other axes. From the simulation, it is also noted that the damping coefficient  $d_s$  doesn't influence the overall performance significantly, so no conductive sheet is placed on the secondary stage finally for simplicity.

## V. EXPERIMENTAL EVALUATION AND DISCUSSION

The prototype of the proposed maglev dual-stage system is shown in Fig. 7. The primary maglev stage and secondary flexure stage are controlled by a National Instruments (NI) PXI-8110 real-time controller with a sampling rate of 5 kHz. Lion Precision capacitive sensors are utilized for the primary maglev stage, and one channel of Renishaw fibre optic laser interferometer is used for the flexure secondary stage. The primary and secondary stages are actuated by the TRUST TA320 and TA115 linear current amplifiers. Fig. 8 plots the open-loop frequency response of the secondary flexure system up to 1000 Hz, where the static case is that the secondary

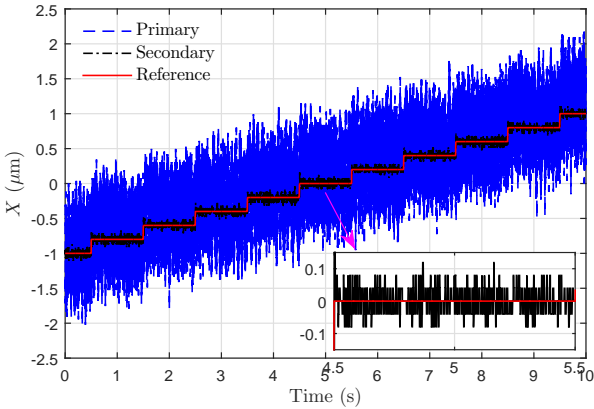


Fig. 9. Positioning resolution evaluation of the maglev dual-stage system using a series of 200 nm steps.

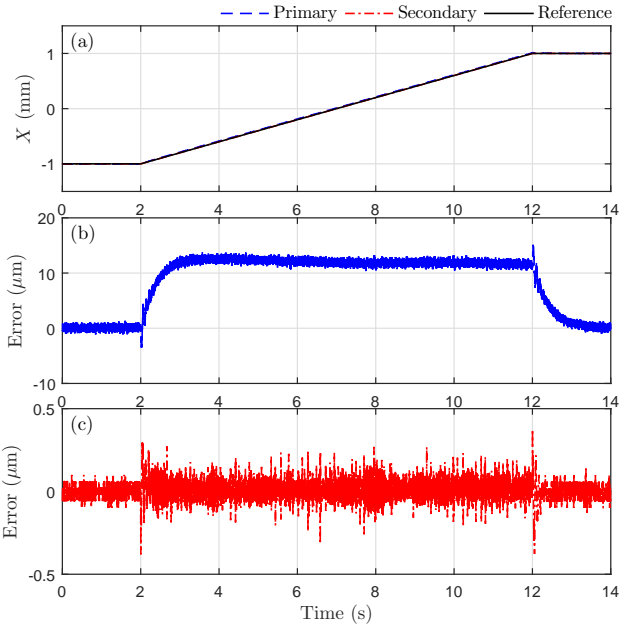


Fig. 10. (a) 2 mm X-axis linear motion under a constant 0.2 mm/s velocity with recorded error of (b) primary stage and (c) secondary stage.

stage is mounted on the ground and tested individually, and the levitated case is that the secondary stage is mounted on the primary stage and tested when the maglev translator is levitated and served on a constant position. From Fig. 8, it can be seen that when the primary stage is levitated up, the frequency response of secondary stage is slightly changed due to the coupling between two stages.

Although many advanced control methods [20], [29] are applicable to the primary maglev stage, the PID controllers are utilized in this work for their robustness and simplicity in all six channels. The parameters for PID controller  $K_p + K_i s^{-1} + K_d s$  in the  $X$  and  $Y$ -axis motions are given as  $K_p = 63$ ,  $K_i = 42$ , and  $K_d = 0.08$  to achieve a closed-loop bandwidth around 20 Hz, which are also similar to other axes. The controller parameters for the secondary stage follows (28), and all controllers are implemented in digital forms by the  $z$ -transform. Fig. 9 shows

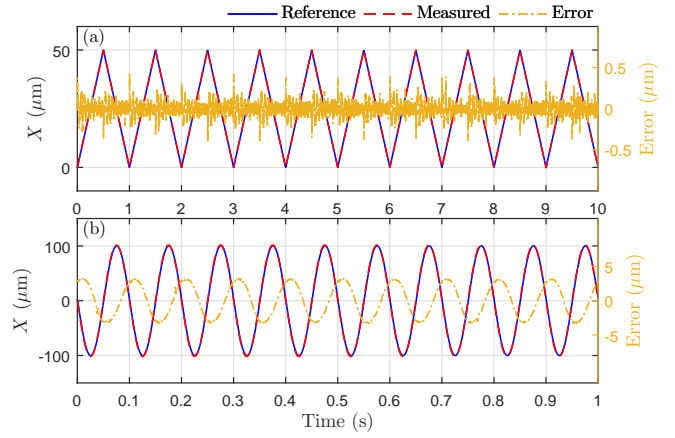


Fig. 11. Tracking performance of (a) 1 Hz triangular reference and (b) 10 Hz sinusoidal reference.

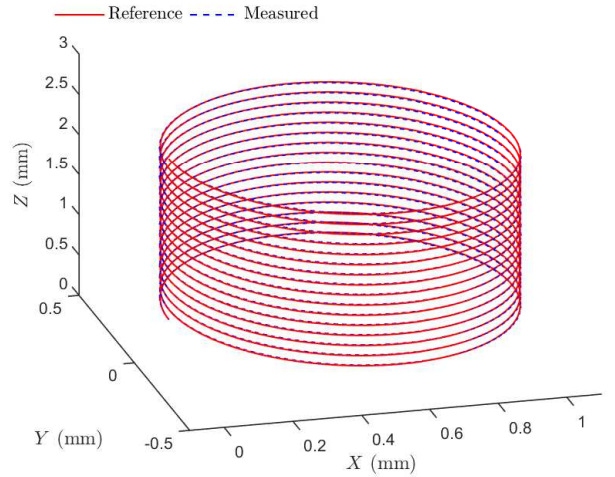


Fig. 12. Tracking performance of 3D helical motion.

the positioning resolution of maglev dual-stage system using a series of 200 nm steps, where both the position signals of the primary and secondary stages are plotted. It can be observed that the Root Mean Square Error (RMSE) of the primary and secondary stages are 413 nm and 43 nm, respectively, which indicates that the secondary stage can effectively compensate the primary stage's vibration and achieve almost the sensor resolution. Furthermore, it is noted static positioning RMSE of the proposed dual-stage is even better than the single-stage maglev positioning system [16] all using laser interferometers, which is around 50 nm. Fig. 10 shows a 2 mm X-axis linear motion with a constant velocity, where both the primary and secondary errors are plotted. From Fig. 10, it can be seen that the dual-stage system can keep the motion error below 200 nm with an RMSE of 51 nm, which is just slightly higher than the static positioning.

The 1 Hz triangular and 10 Hz sinusoidal references are evaluated in the Fig. 11, where the RMSEs are 74 nm and 2.3 μm, respectively. It is also noted that, for the 10Hz sinusoidal reference, the dual-stage positioning performance

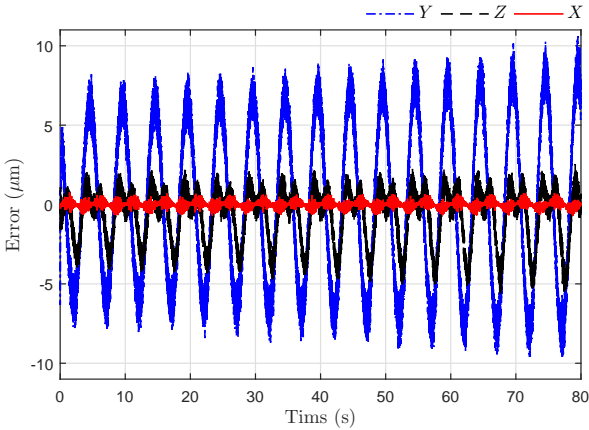


Fig. 13. Recorded error signals for the 3D helical motion.

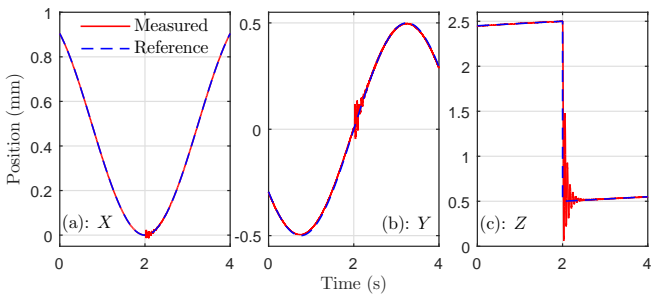


Fig. 14. Robustness evaluation of the maglev system using a 2 mm sudden jump in levitation height during the 3D helical motion.

is much better than the single-stage maglev positioning system [16], as plotted in the Fig. 1(b), the error attenuation rate is significantly improved from -7.2 dB to -30.2 dB. Next, the multi-axis positioning is also evaluated in Fig. 12, where a 3D helical reference is utilized that the  $X$  and  $Y$  axes are conducting circular motion while the levitation  $Z$ -axis is rising from 0.5 mm to 2.5 mm. The error signals of the 3D helical motion are also recorded and plotted in Fig. 13. It is observed that the error signals are continuously increasing in a slow rate, this is due to the decreasing of magnetic field when increasing the levitation height. To evaluate the robustness of the closed-loop maglev dual-stage system, a 2 mm sudden jump from 2.5 mm to 0.5 mm in  $Z$ -axis is tested during the 3D helical motion, which occurs at the 2nd seconds in Fig. 14. It is observed that a large oscillation occurred in all axes due to the sudden jump, however, the maglev system is still stable and able to regulate it into equilibrium in short time. Furthermore, it shows that the oscillation in  $X$  is much slighter than  $Y$ , which demonstrates that the dual-stage axis has much stronger disturbance rejection ability due to the broader closed-loop bandwidth.

Finally, the complementary sensitivity transfer function of the maglev dual-stage system, which related to the reference tracking performance, are experimentally measured and plotted in Fig. 15, which is measured by giving reference with frequency ranged from 1 Hz to 1000 Hz in 200 points to the dual-stage system to track, and concurrently records

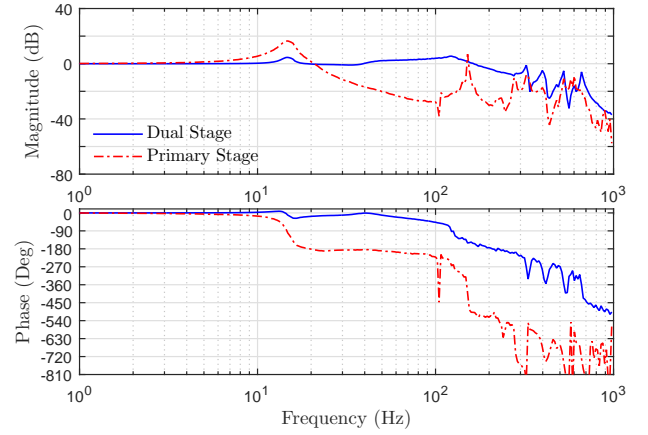


Fig. 15. Experimentally measured closed-loop tracking transfer function of the maglev dual-stage system.

the real positions of primary and secondary stages to obtain the magnitude and phase information for both the primary and dual-stage systems. Fig. 15 indicates that the dual-stage system can achieve about 200 Hz (cross -3 dB). It can be seen that there is a hump appearing between 10 Hz and 20 Hz in the dual-stage tracking transfer function, and this results from the closed-loop resonant mode of the primary stage. To bypass this issue, reference shaping can be utilized to filter the reference signal with a low-pass filter and then feed it to the primary stage, so that the primary stage will only handle the low-frequency signal, and then let the secondary stage can compensate the remaining error in both low and high frequency, which will not go into details in this work.

## VI. CONCLUSION

In this work, the maglev dual-stage system is proposed to improve the bandwidth of the maglev positioning by utilizing flexure-based parallel actuation design, which owns the merits of truly cable-less and reduced levitating mass. Due to the free-floating property of the maglev motion, the design of secondary stage in maglev dual-stage system is important, and to solve this issue, an integrated design approach is proposed to consider various specifications systematically, e.g., robust stability, robust performance, and saturation avoidance under the framework. Through this approach, both the plant modal parameters, e.g. stiffness and damping, and controller parameters of the secondary stage can be solved with guaranteed specifications. The experimental verifications are extensively conducted and our results show that the RMSE of the proposed maglev dual-stage positioning system can achieve 43 nm in the principal axis, and the proposed maglev dual-stage system can significantly improve the closed-loop bandwidth of the maglev positioning/motion to around 200 Hz.

## REFERENCES

- [1] L. Yan, I. M. Chen, C. K. Lim, G. Yang, and K. M. Lee, "Modeling and iron-effect analysis on magnetic field and torque output of electromagnetic spherical actuators with iron stator," *IEEE/ASME Transactions on Mechatronics*, vol. 17, no. 6, pp. 1080–1087, Dec 2012.

- [2] J. Ma, S.-L. Chen, N. Kamaldin, C. S. Teo, A. Tay, A. A. Mamun, and K. K. Tan, "A novel constrained h2 optimization algorithm for mechatronics design in flexure-linked biaxial gantry," *ISA Transactions*, vol. 71, pp. 467 – 479, 2017.
- [3] X. Lu and I. Usman, "6D direct-drive technology for planar motion stages," *CIRP Annals - Manufacturing Technology*, vol. 61, no. 1, pp. 359–362, 2012.
- [4] H. Zhang, B. Kou, Y. Jin, and H. Zhang, "Modeling and analysis of a new cylindrical magnetic levitation gravity compensator with low stiffness for the 6-DOF fine stage," *IEEE Transactions on Industrial Electronics*, vol. 62, no. 6, pp. 3629–3639, June 2015.
- [5] Y. M. Choi and D. G. Gweon, "A high-precision dual-servo stage using halbach linear active magnetic bearings," *IEEE/ASME Trans. Mechatronics*, vol. 16, no. 5, pp. 925–931, Oct. 2011.
- [6] M. Miyasaka and P. Berkelman, "Magnetic levitation with unlimited omnidirectional rotation range," *Mechatronics*, vol. 24, no. 3, pp. 252–264, Apr. 2014.
- [7] R. Fesperman, O. Ozturka, R. Hockena, S. D. Rubenb, T. C. Tsaoob, J. Phippsa, T. Lemmonsa, J. Briena, and G. Caskeya, "Multi-scale alignment and positioning system - MAPS," *Precision Engineering*, vol. 36, no. 4, pp. 517–537, Oct. 2012.
- [8] J. Zhang and C.-H. Menq, "Six-axis magnetic levitation and motion control," *IEEE Trans. Robot.*, vol. 23, no. 2, pp. 196–205, Apr. 2007.
- [9] V. H. Nguyen and W.-J. Kim, "Novel electromagnetic design for a precision planar positioner moving over a superimposed concentrated-field magnet matrix," *IEEE Trans. Energy Convers.*, vol. 27, no. 1, pp. 52–62, Mar. 2012.
- [10] V. H. Nguyen and W. Kim, "Two-phase lorentz coils and linear halbach array for multiaxis precision-positioning stages with magnetic levitation," *IEEE/ASME Transactions on Mechatronics*, vol. 22, no. 6, pp. 2662–2672, Dec 2017.
- [11] W. J. Kim, D. L. Trumper, and J. H. Lang, "Modeling and vector control of planar magnetic levitator," *IEEE Trans. Ind. Appl.*, vol. 34, no. 6, pp. 1254–1262, Nov. 1998.
- [12] T. J. Teo, H. Zhu, and C. K. Pang, "Modeling of a two degrees-of-freedom moving magnet linear motor for magnetically levitated positioners," *IEEE Trans. Magn.*, vol. 50, no. 12, p. 8300512, Dec. 2014.
- [13] W. J. Kim, *High-precision planar magnetic levitation*. Cambridge, MA: Ph.D. dissertation, Dept. Elect. Eng. Comput. Sci., Mass. Inst. Technol., Jun. 1997.
- [14] J. Boeij, E. Lomonova, and A. Vandenput, "Modeling ironless permanent-magnet planar actuator structures," *IEEE Trans. Magn.*, vol. 42, no. 8, pp. 2009–2016, Aug. 2006.
- [15] J. W. Jansen, C. M. M. van Lierop, E. Lomonova, and A. Vandenput, "Modeling of magnetically levitated planar actuators with moving magnets," *IEEE Trans. Magn.*, vol. 43, no. 1, pp. 15–25, Jan. 2007.
- [16] H. Zhu, T. J. Teo, and C. K. Pang, "Design and modeling of a six-degree-of-freedom magnetically levitated positioner using square coils and 1-D Halbach arrays," *IEEE Trans. Ind. Electron.*, vol. 64, no. 1, pp. 440–450, Jan 2017.
- [17] T. Hu and W. J. Kim, "Extended range six-DOF high-precision positioner for wafer processing," *IEEE/ASME Transactions on Mechatronics*, vol. 11, no. 6, pp. 682–689, Dec 2006.
- [18] P. Estevez, A. Mulder, and R. M. Schmidt, "6-DoF miniature maglev positioning stage for application in haptic micro-manipulation," *Mechatronics*, vol. 22, no. 7, pp. 1015 – 1022, 2012.
- [19] H. Shakir and W. J. Kim, "Nanoscale path planning and motion control with maglev positioners," *IEEE/ASME Transactions on Mechatronics*, vol. 11, no. 5, pp. 625–633, Oct 2006.
- [20] S. D. Ruben and T. C. Tsao, "Real-time optimal commutation for minimizing thermally induced inaccuracy in multi-motor driven stages," *Automatica*, vol. 48, no. 8, pp. 1566–1574, Aug. 2012.
- [21] C. Hu, Z. Wang, Y. Zhu, M. Zhang, and H. Liu, "Performance-oriented precision LARC tracking motion control of a magnetically levitated planar motor with comparative experiments," *IEEE Transactions on Industrial Electronics*, vol. 63, no. 9, pp. 5763–5773, Sept 2016.
- [22] J. Ma, S. L. Chen, N. Kamaldin, C. S. Teo, A. Tay, A. A. Mamun, and K. K. Tan, "Integrated mechatronic design in the flexure-linked dual-drive gantry by constrained linear quadratic optimization," *IEEE Transactions on Industrial Electronics*, vol. 65, no. 3, pp. 2408–2418, March 2018.
- [23] H. Zhu, T. J. Teo, C. K. Pang, and W. Liang, "Integrated design of a secondary stage for magnetically levitated dual-stage positioning system," in *2017 IEEE International Conference on Advanced Intelligent Mechatronics (AIM)*, July 2017, pp. 1340–1345.
- [24] K. Bai and K. M. Lee, "Direct field-feedback control of a ball-joint-like permanent-magnet spherical motor," *IEEE/ASME Transactions on Mechatronics*, vol. 19, no. 3, pp. 975–986, June 2014.
- [25] T. Tuma, A. Sebastian, J. Lygeros, and A. Pantazi, "The four pillars of nanopositioning for scanning probe microscopy: The position sensor, the scanning device, the feedback controller, and the reference trajectory," *IEEE Control Systems*, vol. 33, no. 6, pp. 68–85, Dec 2013.
- [26] A. Karimi, H. Khatibi, and R. Longchamp, "Robust control of polytopic systems by convex optimization," *Automatica*, vol. 43, no. 8, pp. 1395–1402, August 2007.
- [27] T. Iwasaki and S. Hara, "Generalized KYP lemma: unified frequency domain inequalities with design applications," *IEEE Transactions on Automatic Control*, vol. 50, no. 1, pp. 41–59, January 2005.
- [28] C. Scherer, P. Gahinet, and M. Chilali, "Multiobjective output-feedback control via LMI optimization," *IEEE Transactions on Automatic Control*, vol. 42, no. 7, pp. 896–911, July 1997.
- [29] X. Li, S. L. Chen, C. S. Teo, and K. K. Tan, "Data-based tuning of reduced-order inverse model in both disturbance observer and feedforward with application to tray indexing," *IEEE Transactions on Industrial Electronics*, vol. 64, no. 7, pp. 5492–5501, July 2017.



**Haiyue Zhu** (S'13–M'17) received the B.Eng. degree in automation from the School of Electrical Engineering and Automation and the B. Mgt. degree in business administration from the College of Management and Economics, Tianjin University, Tianjin, China, in 2010, and the M.Sc. and Ph.D. degrees from the National University of Singapore (NUS), Singapore, in 2013 and 2017, respectively, both in electrical engineering.

He joined the Singapore Institute of Manufacturing Technology (SIMTech), Agency for Science, Technology, and Research (A\*STAR) since 2017, and his current research interests include mechatronics and intelligent robotic systems, etc.



**Tat Joo Teo** (M'08) received the B. Eng. degree in mechatronics engineering from Queensland University of Technology, Australia, in 2003 and the Ph.D. degree from Nanyang Technological University, Singapore, in 2009.

He is with Singapore Institute of Manufacturing Technology as a researcher since 2010 and was a visiting scientist in Massachusetts Institute of Technology in 2016. His research interest is to explore the fundamentals of Newtonian mechanics, solid mechanics, kinematics, and electromagnetism to develop high precision mechatronics or robotic systems for micro-/nano-scale manipulation and biomedical applications.

Dr. Teo has published over 40 peer-reviewed articles and has 4 patents granted. In 2013, he received the IECON Best Paper Award in the theory and servo design category. In 2014, he became the first Singaporean to win the R&D 100 Award, which is the most prestigious international award for technologically-significant products. He currently serves as an Associate Editor for *Nanoscience and Nanotechnology Letters*.



**Chee Khiang Pang, Justin** (S'04–M'07–SM'11) received the B.Eng.(Hons.), M.Eng., and Ph.D. degrees in 2001, 2003, and 2007, respectively, all in electrical and computer engineering, from National University of Singapore (NUS). In 2003, he was a Visiting Fellow in the School of Information Technology and Electrical Engineering (ITEE), University of Queensland (UQ), St. Lucia, QLD, Australia. From 2006 to 2008, he was a Researcher (Tenure) with Central Research Laboratory, Hitachi Ltd., Kokubunji, Tokyo, Japan. In 2007, he was a Visiting Academic in the School of ITEE, UQ, St. Lucia, QLD, Australia. From 2008 to 2009, he was a Visiting Research Professor in the Automation & Robotics Research Institute (ARRI), University of Texas at Arlington (UTA), Fort Worth, TX, USA. From 2009 to 2016, he was an Assistant Professor in Department of Electrical and Computer Engineering (ECE), NUS, Singapore. Currently, he is an Assistant Professor (Tenure) in Engineering Cluster, Singapore Institute of Technology, Singapore. He is an Adjunct Assistant Professor of NUS, Senior Member of IEEE, and a Member of ASME. He is also the Chairman of IEEE Control Systems Chapter of Singapore.

His research interests are on data-driven control and optimization, with realistic applications to robotics, mechatronics, and manufacturing systems.

Dr. Pang is an author/editor of 4 research monographs including *Intelligent Diagnosis and Prognosis of Industrial Networked Systems* (CRC Press, 2011), *High-Speed Precision Motion Control* (CRC Press, 2011), *Advances in High-Performance Motion Control of Mechatronic Systems* (CRC Press, 2013), and *Multi-Stage Actuation Systems and Control* (CRC Press, 2018). He is currently serving as an Executive Editor for *Transactions of the Institute of Measurement and Control*, an Associate Editor for *Asian Journal of Control*, *IEEE Control Systems Letters*, *Journal of Defense Modeling & Simulation*, and *Unmanned Systems*, and on the Conference Editorial Board for IEEE Control Systems Society (CSS). In recent years, he also served as a Guest Editor for *Asian Journal of Control*, *International Journal of Automation and Logistics*, *International Journal of Systems Science*, *Journal of Control Theory and Applications*, and *Transactions of the Institute of Measurement and Control*. He was the recipient of The Best Application Paper Award in The 8th Asian Control Conference (ASCC 2011), Kaohsiung, Taiwan, 2011, and the Best Paper Award in the IASTED International Conference on Engineering and Applied Science (EAS 2012), Colombo, Sri Lanka, 2012.